RSC Advances

PAPER

View Article Online
View Journal | View Issue

Cite this: *RSC Adv.*, 2026, **16**, 275

Molybdenum-doped $La_{0.7}Sr_{0.3}MnO_3$ nanoparticles: tuning magnetic and heating properties for magnetic hyperthermia

Jihed Makni,[a] Kalthoum Riahi, *[b] Mayssa Yengui[c] and Wissem Cheikhrou-Koubaa[d]

Self-limited magnetic hyperthermia offers a promising approach for cancer therapy by exploiting materials whose Curie temperature (T_C) intrinsically constrains overheating during treatment. In this work, ultrafine $La_{0.7}Sr_{0.3}Mn_{1-x}Mo_xO_3$ (x = 0.10, 0.15, 0.20) nanoparticles were synthesized *via* the glycine–nitrate process. All samples crystallized in a rhombohedral ($R\bar{3}c$) structure, with particle size decreasing from ~230 nm to ~105 nm as Mo content increased. Magnetic measurements revealed ferromagnetic–paramagnetic transitions with decreasing T_C. The substitution of Mo^{6+} for Mn^{3+}/Mn^{4+} disrupted double-exchange interactions and altered the Mn^{3+}/Mn^{4+} balance, leading to reduced magnetization and a progressive decrease in T_C (from 350 to 290 K). Under an alternating magnetic field, the nanoparticles exhibited rapid initial heating followed by a plateau near T_C, demonstrating self-limited heating behavior. Specific absorption rate values were moderate (~14–16 W g^{-1} for intermediate doping and ~7 W g^{-1} at the highest doping), consistent with magnetic dilution and surface spin effects. These results show that $La_{0.7}Sr_{0.3}Mn_{1-x}Mo_xO_3$ nanoparticles possess intrinsically self-limited heating suggesting their promise for magnetic hyperthermia. Further fine-tuning Mo doping, particle size, and surface properties could more precisely adjust the Curie temperature and enhance heating efficiency, advancing these nanoparticles toward safe and effective hyperthermia applications.

Received 13th November 2025
Accepted 15th December 2025

DOI: 10.1039/d5ra08765a

rsc.li/rsc-advances

1. Introduction

Since the first demonstration of lymph nodes heating with maghemite nanoparticles, magnetic nanoparticles (MNPs) have attracted growing interest in magnetic fluid hyperthermia (MFH) for cancer therapy.[1] Magnetic hyperthermia has progressed from experimental models to clinical applications, particularly through the development of NanoTherm® therapy by MagForce AG. In this approach, superparamagnetic iron oxide nanoparticles are directly injected into the tumor and subsequently exposed to an alternating magnetic field, producing localized heat within the malignant tissue while sparing surrounding healthy regions. Preclinical and clinical studies in patients with Glioblastoma Multiforme have confirmed the safety, feasibility, and therapeutic benefit of this method, ultimately leading to its European medical approval.[2,3] The performance of magnetic nanoparticles for hyperthermia applications depends on several key factors, including high specific absorption rate (SAR), biocompatibility, chemical stability, low toxicity, and size control. The most widely studied materials are iron oxides (*e.g.*, Fe_3O_4, γ-Fe_2O_3), due to their good biocompatibility. A major limitation of conventional Fe_3O_4-based magnetic mediators is the lack of precise temperature control during treatment of internal tumors.[4,5] Uneven particle distribution can lead to overheating and unintended damage to surrounding healthy tissue. This limitation can be overcome by developing smart magnetic mediators with appropriately low T_C.[6] As the temperature approaches T_C, the particles gradually lose their ferromagnetic ordering and the heat generation under an alternating magnetic field (AMF) diminishes. Upon cooling, magnetization is restored, allowing heating to resume. This reversible behavior enables a self-regulating hyperthermia effect, ensuring intrinsic temperature control during treatment. The T_C of magnetic nanoparticles is an intrinsic parameter that determines the theoretical self-limiting temperature for hyperthermia, while the maximum temperature reached (T_{max}) is the actual experimental outcome of heating under an alternating magnetic field. In self-limited magnetic hyperthermia, T_C is engineered to be within the therapeutic range (≈42–46 °C) so that once the nanoparticles reach this temperature they lose magnetization and stop heating, thereby preventing overheating of healthy tissue. Magnetic nanoparticles can exhibit either self-limited or self-regulated heating: in the former,

[a]*Laboratory of Chemistry, Materials and Modelling (LR24ES02), Preparatory Institute for Engineering Studies of Kairouan, University of Kairouan, Tunisia. E-mail: kalthoumriahi@gmail.com*

[b]*Faculty of Science of Sfax, University of Sfax, Tunisia*

[c]*ECAM Louis de Broglie, Campus de Ker Lann – CS 29128 – 35091 RENNES Cedex9, France*

[d]*Centre de Recherche en Numérique de Sfax, Technopole de Sfax, B.P. 275, 3021, Sfax, Tunisia*

temperature rise is intrinsically constrained as T_C is approached, while in the latter, T_C is intentionally adjusted to the therapeutic range, enabling controlled hyperthermia suitable for cancer treatment.[7–9] In recent years, perovskite manganites with the general formula $La_{1-x}A_xMnO_3$ (A = Sr, Ba, Ca) have attracted considerable attention due to their tunable magnetic transition temperature and enhanced magnetic anisotropy.[10] By adjusting the doping level x, T_C can be set within the optimal therapeutic range of 42–45 °C (315.15–318.15 K), ideal for magnetic hyperthermia. In this range, the T_C can be fine-tuned to sustain heating up to 50 °C, in contrast to superparamagnetic iron oxide nanoparticles (SPIONs) with $T_C \approx 823$ K, thereby enabling effective thermal control without altering the AMF.[11] At this point, the particles undergo a transition to the paramagnetic state, stopping overheating and thereby preventing tissue damage. When synthesized at nanoscale dimensions (typically 20–100 nm) with controlled morphology and anisotropy, $La_{0.7}Sr_{0.3}MnO$ (LSMO) nanoparticles can generate heat efficiently under alternating magnetic fields. This combination of efficient heating and inherent self-limiting behavior makes them promising materials for safe and magnetic hyperthermia treatments.[6,12] In their report, Pashchenko *et al.*[13] reported that nanoparticles $La_{0.6}Ag_{0.2}Mn_{1.2}O_3$ with a Curie temperature of 315–317 K can act as self-regulating "smart" materials in magnetic hyperthermia, preventing overheating by ceasing heat generation once this threshold is reached. Partial substitution of Mn with transition metals such as Mo and Ti has been shown to adjust magnetic and electrical properties, thereby influencing heating performance under an AMF.[14,15] Ferrites (MFe_2O_4; M = Co, Mn, Zn, *etc.*) offer tunable magnetic properties but their hyperthermic efficiency strongly depends on their composition and synthesis method.[16] Recently, Murugan *et al.* reported that Zr^{4+} doping in La^{3+}-substituted lanthanum strontium manganite nanoparticles effectively tunes their magnetic and thermal properties for magnetic hyperthermia. The incorporation of Zr^{4+} induces lattice distortion and modifies the Mn^{3+}/Mn^{4+} ratio, resulting in a reduced Curie temperature (~317 K) within the therapeutic range and improved heating efficiency. These effects highlight the potential of Zr^{4+}-doped LSMO as a biocompatible, self-regulating agent for targeted cancer hyperthermia.[17] Similarly, Ahmad *et al.* reported that the SAR of Gd-doped LSMO nanoparticles decreases with increasing Gd content, with $La_{0.58}Sr_{0.27}Gd_{0.15}MnO_3$ exhibiting a self-limited hyperthermia temperature of ~44.5 °C below T_C, demonstrating controlled heating suitable for therapy.[18] In another approach, Shlapa *et al.*[19] showed that Fe-doped LSMO nanoparticles in agarose solutions generate heat efficiently only below their Curie temperature, emphasizing that fine-tuning T_C allows safe control of maximum heating. Building on these findings, in our previous work, we synthesized $La_{0.7}Sr_{0.3}MnO_3$ and Mo- and Ti-doped derivatives *via* an aqueous combustion method, achieving mean crystallite sizes of ~18 nm. The SAR values measured for these samples confirmed that doping can slightly modulate heating efficiency, consistent with the trend observed in other doped LSMO systems.[20] However, unlike Ti, Zr, or Gd dopants, whose effects primarily arise from structural distortion or magnetic dilution, Mo introduces mixed-valence Mo^{4+}/Mo^{6+} species that directly modify the double-exchange pathway. This results in a more predictable and continuous tuning of T_C and, importantly, enables the emergence of a robust self-limited heating behavior under AMF. Such a self-regulating effect has not been consistently reported in Ti-, Zr-, or Gd-doped systems, suggesting that Mo substitution may offer an additional mechanism to achieve controlled heating behavior in LSMO-based hyperthermia materials.

In this study, we expand on previous work by investigating $La_{0.7}Sr_{0.3}MnO_3$ (LSMO) nanoparticles doped with varying fractions of molybdenum (Mo), synthesized *via* the glycine-nitrate process (GNP). This wet-chemical method is cost-effective, scalable, and allows precise compositional control and homogeneity at the nanoscale, enabling the formation of single-phase nanoparticles with controlled size and morphology, which are critical for magnetic hyperthermia performance.[21] The choice of Mo as a dopant in $La_{0.7}Sr_{0.3}MnO_3$ was motivated by its unique ability to adopt multiple oxidation states (Mo^{4+}/Mo^{6+}), which allows fine tuning of the Mn^{3+}/Mn^{4+} ratio and the double-exchange interactions that govern magnetic behavior. This enables a controllable reduction of the Curie temperature (T_C), a key parameter for achieving self-limited magnetic hyperthermia. Additionally, the moderate ionic size of Mo^{4+}/Mo^{6+} relative to Mn^{3+}/Mn^{4+} introduces lattice strain that can reduce particle size and improve heating efficiency without significantly destabilizing the rhombohedral perovskite structure.

In this work, we aim to elucidate the role of Mo doping in modifying structural, morphological, and magnetic properties, including lattice parameters, particle size, surface features, saturation magnetization, and coercivity. Additionally, the heating performance under an alternating magnetic field is evaluated through specific absorption rate and thermal response analyses. These investigations provide insights into the potential of Mo-doped LSMO nanoparticles for self-limited magnetic hyperthermia, enabling controlled and safe heat delivery for biomedical applications.

2. Synthesis method

The $La_{0.7}Sr_{0.3}Mn_{1-x}Mo_xO_3$ (x = 0.1, 0.15, and 0.2) particles were synthesized *via* the glycine-nitrate autocombustion method (GNP) in aqueous solution. This method relies on a redox reaction between an oxidizing agent and a fuel. According to the literature, metal nitrates are typically used as oxidants, while common fuels include glycine, urea, or citric acid. In this study, glycine (NH_2CH_2COOH) was chosen as the fuel. A glycine-to-nitrate molar ratio (G/N) of 0.56 was selected to enhance metal ion chelation while maintaining sufficient combustion temperature to initiate crystallization. Stoichiometric amounts of $La(NO_3)_3 \cdot 6H_2O$, $Sr(NO_3)_2 \cdot 4H_2O$, $Mn(NO_3)_2 \cdot 4H_2O$, and glycine ($C_2H_5NO_2$) were dissolved in deionized water. Molybdenum oxide (MoO_3) was dissolved in nitric acid to form a soluble molybdenum nitrate, which was then added to the precursor solution. The mixture was stirred vigorously and heated at 100 °C for 2 hours to evaporate the water, leading to the formation of a transparent viscous gel. The temperature was then increased to

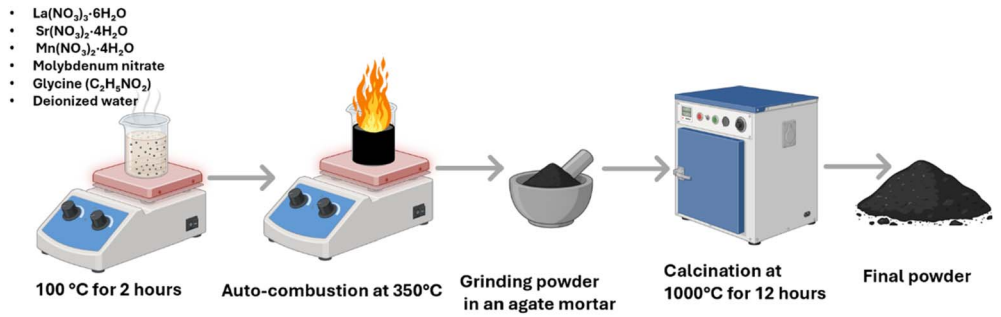

Fig. 1 Glycine-nitrate combustion synthesis of schematic illustration of the synthesis procedure for $La_{0.7}Sr_{0.3}Mn_{1-x}Mo_xO_3$ ($x = 0.1$, 0.15, and 0.2) *via* the glycine–nitrate auto-combustion method. Precursors were dissolved in deionized water with glycine as a fuel and heated at 100 °C for 2 h. The resulting gel underwent auto-combustion at 350 °C, followed by grinding in an agate mortar and calcination at 1000 °C for 12 h to obtain the final powder.

around 350 °C, triggering the auto-combustion process. The resulting reaction produced voluminous black ash, which was ground and subsequently calcined at 1000 °C for 12 hours to improve phase purity and crystallinity. A schematic summary of the preparation process is presented in Fig. 1.

3. Experimental details

The phase and the crystal structure of the synthesized samples were analyzed using Cu K_α radiation with an X-ray diffractometer. The surface morphology and distribution of grain size were evaluated using Scanning Electron Microscopy (SEM). Magnetic measurements were carried out using vibrating sample magnetometer. AC magnetic hyperthermia were performed using a non-adiabatic experimental setup DM100 Series built by a nanoScale Biomagnetic magnetic fluid hyperthermia measuring system. Dependences of heating temperature *versus* time of LSMO NPs were recorded under a magnetic field of 30 mT and three different frequencies (119, 248, and 313 kHz). To calculate the SAR, the heating curve is fitted using the phenomenological Box-Lucas method with the following expression:[22] $\Delta T = a(1 - e^{-b(t-t_0)})$ with a and b as the fitting parameters. a is the initial slope of the heating curve, and b is a constant describing the cooling rate. In this study, the SAR values were calculated directly from the measured heating curves without applying a separate adiabatic correction; however, the Box–Lucas fitting inherently accounts for heat losses *via* the parameter b, which describes the cooling rate of the system. The SAR values are calculated as: $SAR = abC/m_{MNPs}$, where C is the specific heat capacity of $LaSrMnO_3$ ($C = 660$ J kg^{-1} K^{-1}), and m_{MNPs} is the mass of MNPs. The intrinsic loss power parameter (ILP, nH m^2 kg^{-1}) enables normalization of SAR values measured at different frequencies.

4. Structural characterization

X-ray diffraction (XRD) patterns of $La_{0.7}Sr_{0.3}Mn_{1-x}Mo_xO_3$ samples ($x = 0.1$, 0.15, and 0.2), presented in Fig. 2a, reveal that the primary crystalline phase corresponds to the rhombohedral perovskite structure assigned to the $R\bar{3}c$ space group. Phase analysis, carried out using X'Pert HighScore Plus software, identified secondary phases as $La_2Mo_3O_{12}$ with a monoclinic structure ($C\,1\,2/c\,1$) and $SrCO_3$ with a hexagonal structure ($R\bar{3}m$).

Quantitative assessment shows that the proportion of the perovskite phase decreases with increasing Mo content: 88% for $x = 0.1$, 85% for $x = 0.15$, and a marked drop to 62% for $x = 0.2$. This decline is accompanied by an increase in $La_2Mo_3O_{12}$ content from 3% to 31%, while $SrCO_3$ remains relatively constant (9%, 8%, and 7%, respectively). The growth of these secondary phases at higher substitution levels suggests a solubility limit of Mo^{6+} within the LSMO lattice. Once this limit is exceeded, Mo preferentially reacts with La, leading to the formation of the thermodynamically stable $La_2Mo_3O_{12}$ phase. This behavior can also be influenced by the synthesis route employed. The glycine–nitrate auto-combustion method, particularly under sub-stoichiometric glycine-to-nitrate (G/N) ratios, affects the complexation of metal ions. Insufficient glycine may result in incomplete chelation, leading to the precipitation of free cations as carbonate ($SrCO_3$) or oxide ($La_2Mo_3O_{12}$) phases during the heating stages. Interestingly, these secondary phases involve only La, Sr, and Mo, suggesting that Mn ions are preferentially integrated into the perovskite structure due to their stronger interaction with glycine, as previously discussed by Epherre *et al.*,[23] although this contrasts earlier reports by Chick and Peng.[21,24]

Structural refinement was performed by Rietveld analysis using the FullProf suite,[25,26] and the quality of the fit is confirmed by χ^2 values ranging between 1.36 and 1.46, indicating good agreement between the experimental and calculated patterns (Fig. 1b–d). The refined structural model confirms that all samples crystallize in the rhombohedral $R\bar{3}c$ symmetry. The calculated Goldschmidt tolerance factors (t) decrease slightly with increasing Mo substitution (0.9619 for $x = 0.1$, 0.953 for $x = 0.15$, and 0.945 for $x = 0.2$), reflecting a gradual distortion of the perovskite lattice. This trend aligns with the substitution of Mn^{4+} ions (smaller radius) by larger Mo^{6+} and Mn^{2+} ions, causing local lattice expansion and deviation from the ideal cubic configuration.

In addition, the refined lattice parameters and unit cell volumes exhibit slight variations with increasing Mo content, reflecting a minor distortion of the rhombohedral structure. This behavior is consistent with the gradual decrease in the Goldschmidt tolerance

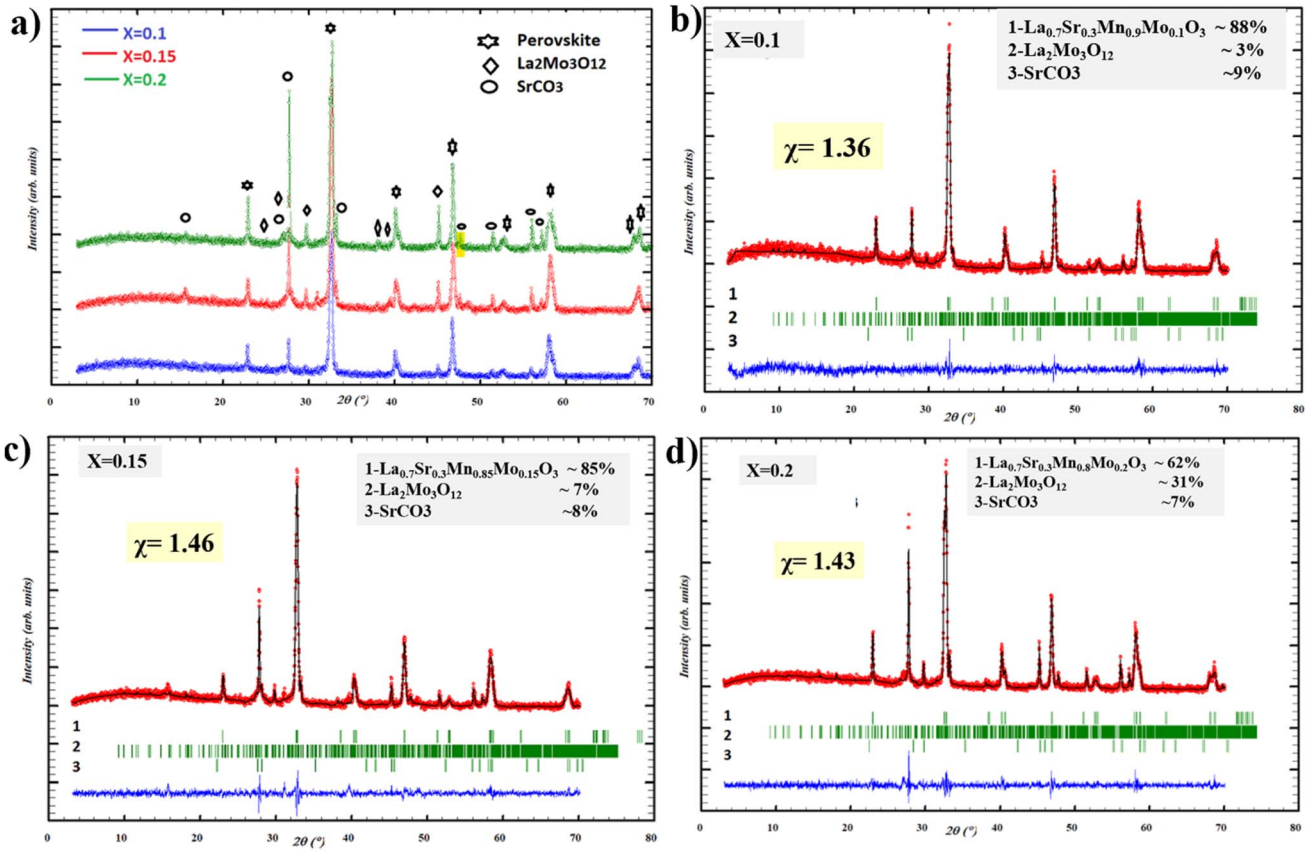

Fig. 2 X-ray diffraction (XRD) patterns and Rietveld refinement results for $La_{0.7}Sr_{0.3}Mn_{1-x}Mo_xO_3$ (x = 0.1; 0.15 and 0.2) (a) comparison of experimental diffraction patterns for the three compositions, showing characteristic peaks of the perovskite phase, $La_2Mo_3O_{12}$, and $SrCO_3$. (b–d) Rietveld refinement profiles for x = 0.10; 0.15, and 0.20, respectively, with phase composition percentages and weighted profile R-factors (χ^2) indicated. The main perovskite phase is dominant across all samples, with increasing secondary phase content observed at higher Mo substitution levels.

factor. The substitution of smaller Mn^{4+} by larger Mo^{6+} and possibly Mn^{2+} ions causes a modest lattice expansion, as evidenced by the increase in unit cell volume. However, the rhombohedral angle α remains nearly unchanged, indicating that the perovskite framework maintains its structural integrity. These results confirm the limited incorporation of Mo into the LSMO lattice and support the observed microstructural stability.

The crystallite sizes were estimated using the Debye–Scherrer formula, applied to the most intense diffraction peak. The equation used is:

$$D = \frac{K\lambda}{\beta\cos\theta} \quad (1)$$

where D is the average crystallite size, K is the Scherrer constant (taken as 0.9), λ is the wavelength of the Cu Kα radiation (1.5406 Å), β is the full width at half maximum (FWHM) of the principal peak, and θ is the corresponding Bragg angle.

The calculated crystallite sizes exhibit a non-monotonic variation with Mo content: 19.24 nm for x = 0.1, 22.49 nm for x = 0.15, and 18.48 nm for x = 0.2. This trend correlates with the phase distribution observed in the Rietveld refinement. At x =

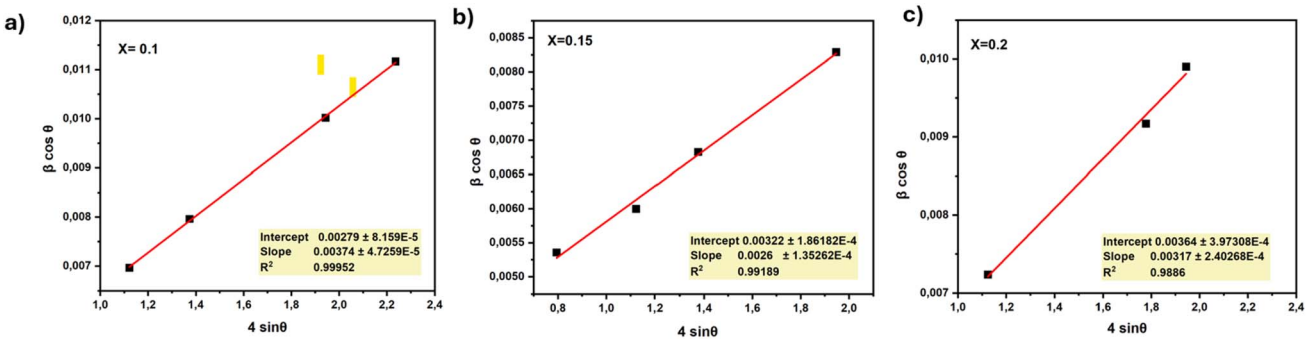

Fig. 3 Williamson–Hall (W–H) plot for $La_{0.7}Sr_{0.3}Mn_{1-x}$ Mo_xO_3 (x = 0.1; 0.15 and 0.2).

Table 1 Structural and microstructural parameters of the compounds with $X = 0.1$, 0.15, and 0.2, including phase fraction, lattice constants, unit cell volume, bond lengths and angles, refinement quality factors, tolerance factor, and particle sizes obtained from Williamson–Hall (W–H) analysis and XRD

Compounds	$X = 0.1$	$X = 0.15$	$X = 0.2$
Space group	$R\bar{3}c$	$R\bar{3}c$	$R\bar{3}c$
% Manganite phase	88	85	62
a (Å)	5.5015	5.4872(3)	5.5040
b (Å)	5.5015	5.4872(3)	5.5040
c (Å)	13.346	13.3503(10)	13.336
V (Å^3)	349.829	348.1154	349.880
$\langle d$ Mn,Mo–O$\rangle$ (Å)	1.95345	1.95200	1.959
$\langle\theta$ Mn,Mo–O–Mn,Mo$\rangle$ (°)	165.985	165.167	163.207
χ^2	1.36	1.46	1.43
R_{bragg}	4.08	2.69	2.76
R_F	2.76	2.47	2.13
t	0.9619	0.9535	0.9453
Particle size from (W–H) (nm)	49.96	43.06	43.73
Particle size from XRD (nm)	19.24	22.49	18.48

0.1, the $La_{0.7}Sr_{0.3}MnO_3$ phase dominates (88%), and the moderate crystallite size reflects minimal structural disruption. The increase to 22.49 nm at $x = 0.15$ suggests improved structural coherence and crystallite growth, likely due to better incorporation of Mo^{6+} ions. However, for $x = 0.2$, a marked decrease in LSMO content to 62%, along with a rise in $La_2Mo_3O_{12}$ and $SrCO_3$ secondary phases, indicates significant structural disorder, which hinders uniform crystallite development and leads to a smaller average size.

To further analyze the microstructure, the Williamson–Hall (W–H) method was applied using the relation,[27] taking into account both crystallite size and strain-induced broadening:

$$\beta \cdot \cos\theta = \frac{K\lambda}{D_{WH}} + 4\varepsilon \cdot \sin\theta \quad (2)$$

where ε is the microstrain and k is the shape factor (0.9).

Linear fits of the W–H plots (Fig. 3) suggest a homogeneous distribution of strain and crystallite size, indicating relatively uniform microstructural characteristics. The extracted crystallite sizes for the rhombohedral phase are 49.96 nm ($x = 0.1$), 43.06 nm ($x = 0.15$), and 43.73 nm ($x = 0.2$). The larger sizes obtained *via* the W–H method compared to those from the Debye–Scherrer equation are attributed to the inclusion of strain effects in the W–H approach, which are not considered in the Scherrer method (Table 1). This discrepancy between the two methods highlights the significant influence of microstrain on peak broadening. Interestingly, while the Debye–Scherrer method yields the smallest size for $x = 0.1$, the W–H method gives the largest crystallite size for the same composition. This

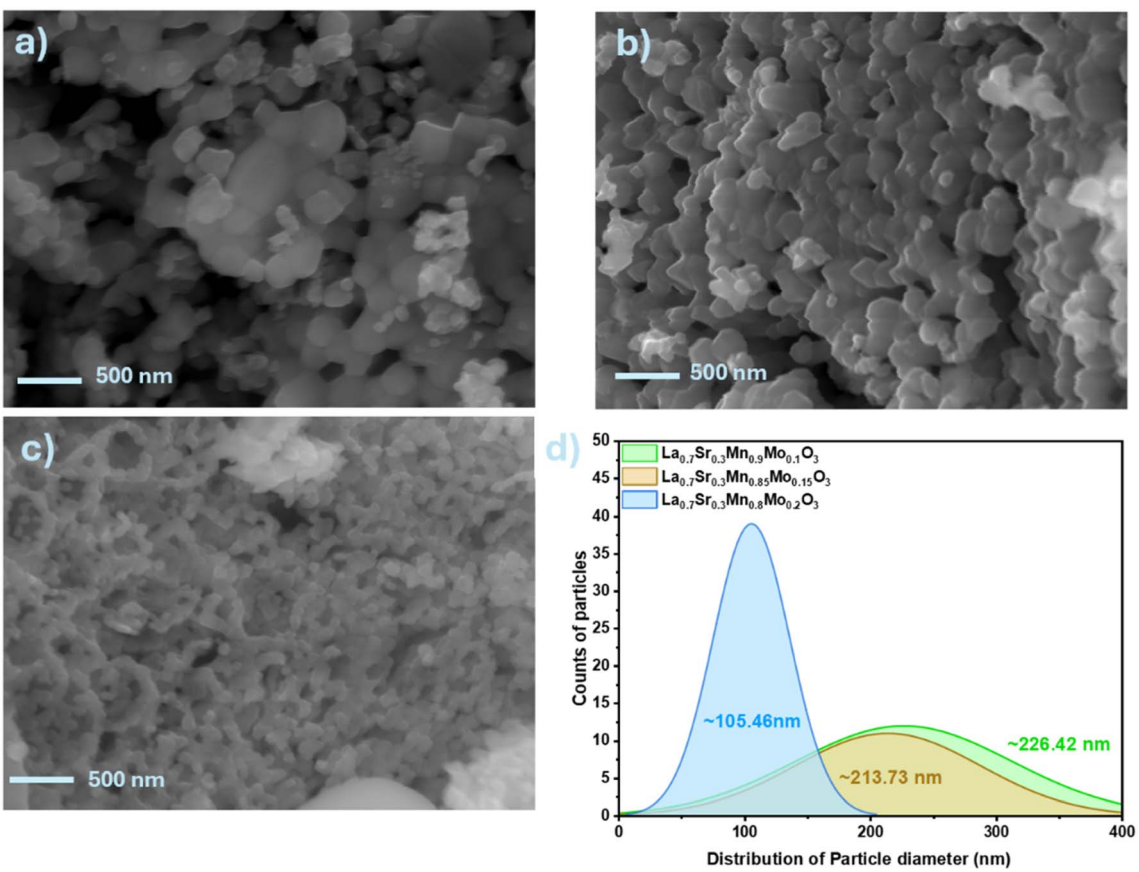

Fig. 4 Scanning electron microscopy (SEM) micrographs of $La_{0.7}Sr_{0.3}Mn_{1-x}Mo_xO_3$ ($x = 0.1$; 0.15 and 0.2), accompanied by particle size distribution histograms. The distributions were obtained by statistical analysis of the SEM images and fitted with a log-normal function to determine the average particle diameter and size distribution.

inverse trend suggests that microstrain effects are more pronounced at higher Mo content. An agglomeration factor (D_{W-H}/D_{XRD}) close to 2 was found for all samples, indicating a moderate degree of particle clustering.

The W–H method yields larger sizes than the Debye–Scherrer method because it separates strain-induced broadening from size broadening. The origin of micro strain is closely linked to Mo substitution. The slightly larger ionic radii of Mo^{4+}/Mo^{6+} compared to Mn^{3+}/Mn^{4+} introduce local lattice distortions in the Mn–O framework, creating heterogeneous strain fields. This effect is compounded at higher Mo contents, where partial formation of secondary phases ($La_2Mo_3O_{12}$, $SrCO_3$) further disrupts the lattice. The non-monotonic trend observed with larger W–H crystallite size at $x = 0.1$ despite a smaller Debye–Scherrer size suggests that microstrain dominates peak broadening at low Mo content, while at higher doping levels, the combination of lattice strain and phase heterogeneity influences both the crystallite size and microstrain. Thus, the microstrain is a direct consequence of Mo doping and the associated lattice distortions, rather than an artifact of measurement or processing.

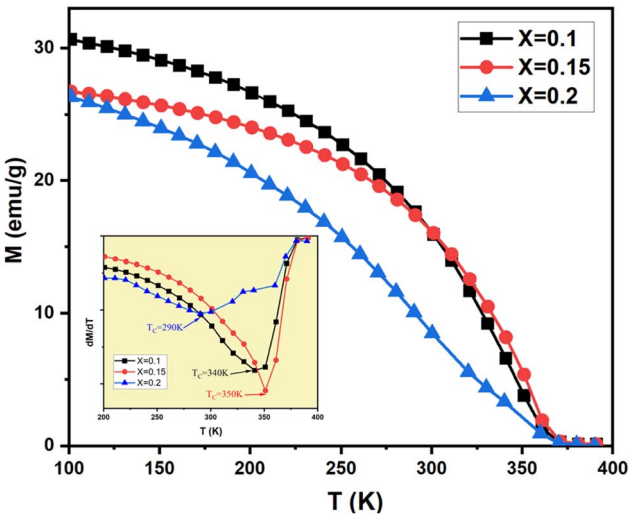

Fig. 5 (a) Temperature dependence of the magnetization, recorded at 0.05 T, for $La_{0.7}Sr_{0.3}Mn_{1-x}Mo_xO_3$ ($x = 0.1$; 0.15 and 0.2) compounds; (b) the plot of dM/dT curve for determining T_C.

Scanning electron microscopy (SEM) images of $La_{0.7}Sr_{0.3}Mn_{1-x}Mo_xO_3$ samples, shown in Fig. 4, reveal a systematic decrease in particle size with increasing Mo doping. The average particle diameters were 226.42 nm, 213.73 nm, and 105.46 nm for $x = 0.1$, 0.15, and 0.2, respectively. Accordingly, the $x = 0.1$ and 0.15 samples can be classified as ultrafine particles, while the $x = 0.2$ sample consists of nanoparticles. This reduction in particle size is primarily attributed to the effect of Mo substitution on the nucleation and growth processes during the auto-combustion synthesis. The slightly larger ionic radii of Mo^{4+}/Mo^{6+} compared to Mn^{3+}/Mn^{4+} (6-coordinate, Shannon radii) introduce local lattice strain, which inhibits particle coalescence and slows grain growth, promoting the formation of smaller crystallites. While segregation of Mo at grain boundaries could theoretically contribute, the rapid and uniform nature of the combustion reaction suggests that nucleation and growth dynamics dominate the particle size evolution. Therefore, the observed decrease in particle size with increasing Mo content reflects the combined influence of lattice strain and modified nucleation and growth processes rather than grain-boundary segregation.

5. Magnetic characterization

All synthesized samples reveal a typical ferromagnetic-to-paramagnetic (FM–PM) transition. A decrease in magnetization with increasing Mo content is observed, indicating the weakening of ferromagnetic interactions due to Mo substitution at the Mn site. The Curie temperatures (T_C), determined from the minima of the dM/dT *vs.* T curves (see the inset), are approximately 340 K for $x = 0.1$, 350 K for $x = 0.15$, and 290 K for $x = 0.2$, reflecting modifications in magnetic coupling strength upon doping (Fig. 5).

Isothermal magnetization curves (M *vs.* μ_0H) measured from 100 K to 390 K (Fig. 6) display well-saturated hysteresis loops at low temperatures for all compositions, confirming robust ferromagnetic ordering. However, the saturation magnetization (M_S) decreases with increasing Mo content (Table 2), likely due to the dilution of Mn^{3+}–O–Mn^{4+} double exchange pathways by nonmagnetic Mo^{6+} ions or the introduction of antiferromagnetic Mo–O–Mn interactions.[28] At high temperatures, the curves become linear, indicating a transition to the paramagnetic regime.

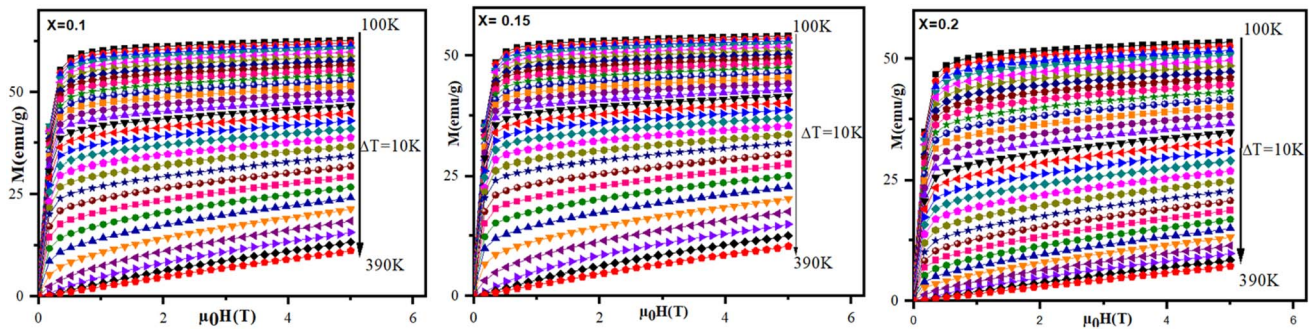

Fig. 6 Isothermal magnetization (M) as a function of the applied magnetic field (μ_0H) at various temperatures for $La_{0.7}Sr_{0.3}Mn_{1-x}Mo_xO_3$ compounds with $x = 0.1$, 0.15, and 0.2.

Table 2 T_C, M_{sat}, M_r, and H_c values for $La_{0.7}Sr_{0.3}Mn_{1-x}Mo_xO_3$ compounds ($x = 0.1$, 0.15, and 0.2) under magnetic applied fields of 2T

Compounds	$X = 0.1$	$X = 0.15$	$X = 0.2$
T_C (K)	340	350	290
M_{sat} (emu g^{-1})	29.44	28.40	2.43
M_r (emu g^{-1})	19	19.3	1.52
H_c (T)	0.064	0.066	0.062

To determine the nature of magnetic phase transition, the Arrott plots (M^2 *vs.* H/M, Fig. 7) have been measured. For all samples, the isotherms exhibit positive slopes at high fields, which, according to the Banerjee criterion, are consistent with a second-order magnetic phase transition.[29] Near T_C, the curvature of the low-field region diminishes and approaches linearity, confirming the FM–PM transition's second-order nature.

The room-temperature hysteresis loops (Fig. 8a) and magnetic parameters summarized in Table 2 reveal the impact of Mo substitution on the magnetic behavior of $La_{0.7}Sr_{0.3}Mn_{1-x}Mo_xO_3$ nanoparticles. At lower Mo content ($x = 0.1$ and 0.15), the samples display clear ferromagnetic behavior with significant saturation magnetization (M_{sat}) and remanent magnetization (Mr). This suggests that the double-exchange interactions between Mn^{3+} and Mn^{4+} ions remain largely intact, allowing robust ferromagnetic ordering. The slight increase in T_C from $x = 0.1$ (340 K) to $x = 0.15$ (350 K) may result from improved incorporation of Mo into the Mn sites, which subtly modifies the Mn^{3+}/Mn^{4+} ratio and strengthens long-range magnetic interactions.

For $x = 0.2$, a sharp decrease in M_{sat} (2.43 emu g^{-1}) and Mr (1.52 emu g^{-1}), accompanied by a reduction in T_C (290 K), indicates that excessive Mo disrupts the double-exchange pathways, weakening ferromagnetic ordering and moving the system toward a paramagnetic-like behavior at room temperature. This is likely due to magnetic dilution as Mo ions are non-magnetic compared to Mn and the formation of secondary phases (as observed previously in XRD results), which further disrupt the Mn–O–Mn.

Interestingly, the coercivity (Hc) remains nearly constant across all compositions (~0.064–0.066 T). This suggests that while Mo substitution strongly affects the magnitude of magnetization and T_C, it does not significantly alter magnetic anisotropy in these particles. The inset of Fig. 8 highlights the progressive reduction in Mr and Hc in the low-field region, reinforcing that Mo doping predominantly weakens ferromagnetic exchange rather than modifying anisotropic contributions.

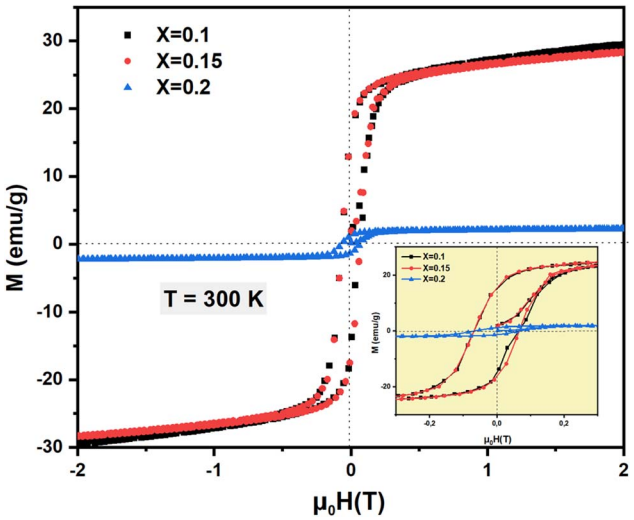

Fig. 8 Hysteresis loops measured at 300 K for $La_{0.7}Sr_{0.3}Mn_{1-x}Mo_xO_3$ compounds ($x = 0.1$, 0.15, and 0.2): (a) full magnetic field range from −2 T to +2 T; (b) magnified view in the low-field region (−0.3 T to +0.3 T) to highlight coercivity and remanence.

Overall, these results demonstrate that moderate Mo doping can tune T_C and magnetic behaviour for potential hyperthermia applications, whereas high Mo content can suppress ferromagnetic ordering, which may limit heating efficiency.

6. AC magnetic hyperthermia

Fig. 8a–c shows the heating curves of $La_{0.7}Sr_{0.3}Mn_{1-x}Mo_xO_3$ ($x = 0.10$, 0.15, and 0.20) under an AC magnetic field of 30 mT at three frequencies (119, 203, and 313 kHz). In all cases, the temperature rises rapidly during the initial stage and then approaches a plateau. The inflection point between these two regimes corresponds to the ferromagnetic–paramagnetic transition, *i.e.*, the Curie temperature (T_C). The shaded region highlights the hyperthermia window (≈41–46 °C), within which therapeutic heating can be achieved. The heating rate clearly increases with

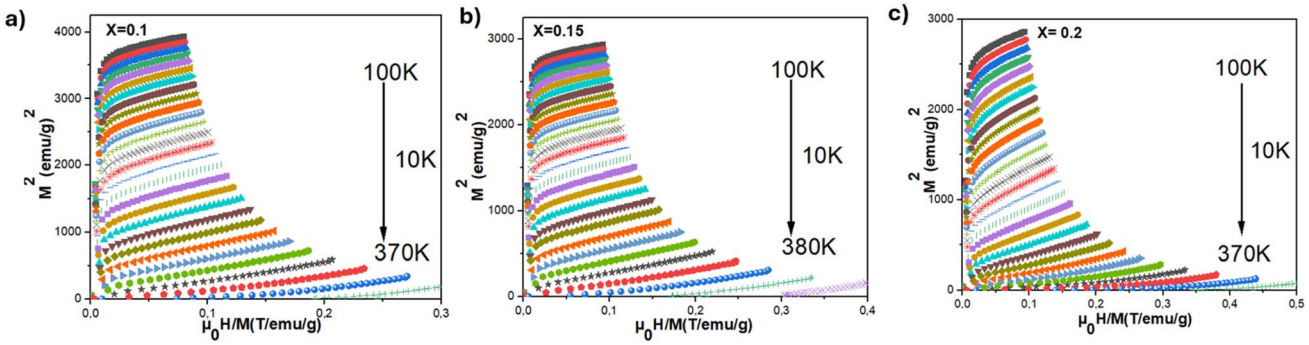

Fig. 7 Arrott plots (M^2 *vs.* H/M) at various temperatures for $La_{0.7}Sr_{0.3}Mn_{1-x}Mo_xO_3$ compounds with $x = 0.1$, 0.15, and 0.2, used to investigate the nature of the magnetic phase transition.

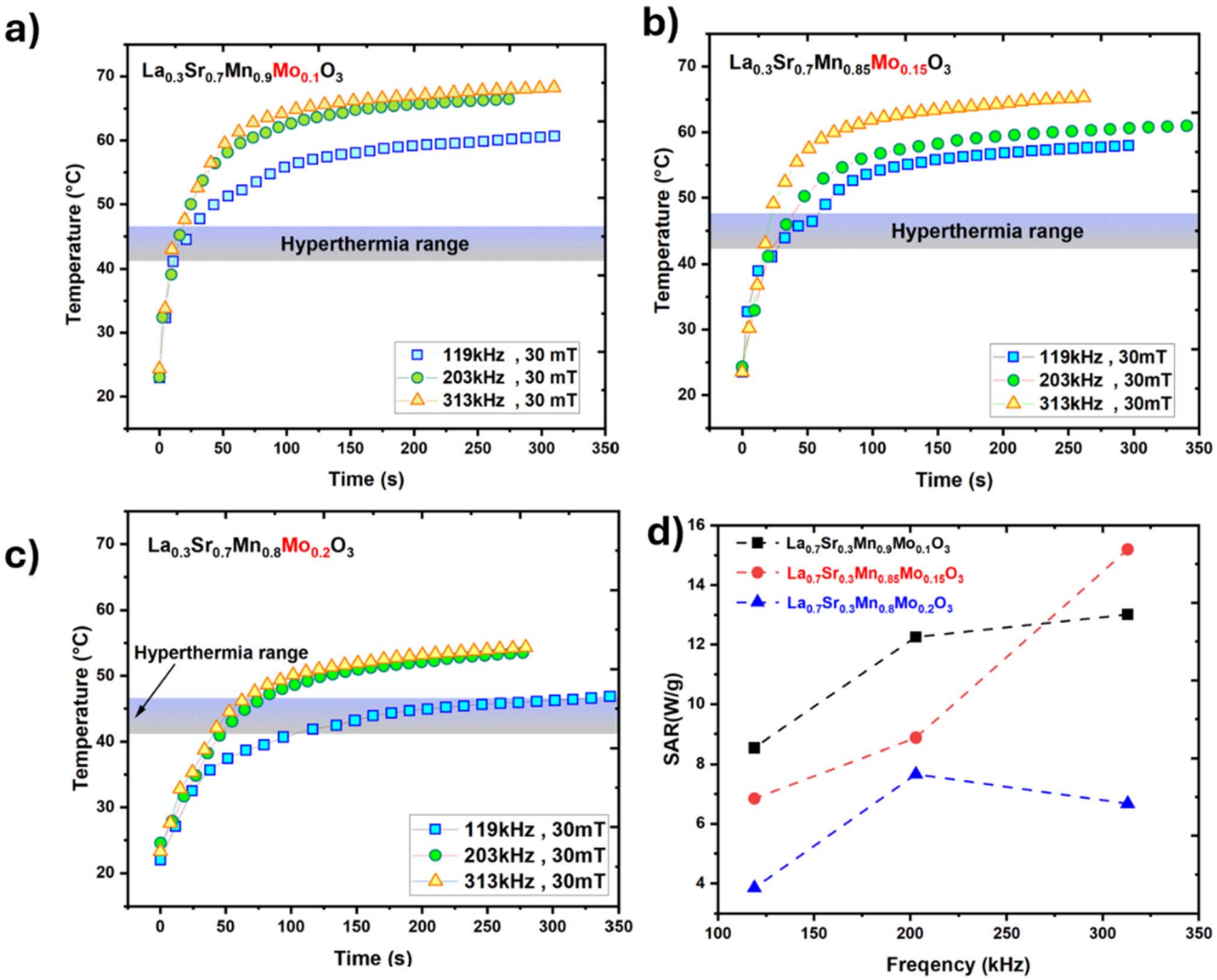

Fig. 9 Magnetic heating performance of $La_{0.7}Sr_{0.3}Mn_{1-x}Mo_xO_3$ under an AC magnetic field of 30 mT at different frequencies. Heating curves for (a) $x = 0.10$, (b) $x = 0.15$, and (c) $x = 0.20$ are shown with the hyperthermia range (41–46 °C) highlighted. (d) Frequency dependence of the specific absorption rate for all samples. Moderate Mo substitution ($x = 0.10$ and 0.15) enhances heating efficiency, yielding higher SAR values and faster attainment of the hyperthermia window, while heavier substitution ($x = 0.20$) suppresses heating due to dilution of the Mn sublattice and reduced Curie temperature.

frequency, consistent with linear response theory (SAR $\propto H^2f$). At 313 kHz, the $x = 0.10$ and 0.15 samples surpass 60 °C, while the $x = 0.20$ sample stabilizes near ~52 °C, just above the hyperthermia range. This trend reflects the influence of Mo substitution on the magnetic exchange interactions: moderate Mo doping ($x = 0.10$–0.15) enhances heating efficiency, while heavier substitution ($x = 0.20$) reduces it, likely due to increased dilution of the Mn sublattice and a corresponding reduction in T_C. The corresponding SAR values (Fig. 8) confirm this behavior. For $x = 0.10$ and 0.15, SAR increases steadily with frequency, reaching maxima of ~14 W g^{-1} and ~16 W g^{-1}, respectively, at 313 kHz. By contrast, the $x = 0.20$ composition shows a significantly lower SAR (~7 W g^{-1} at 313 kHz). These results indicate that the hyperthermia performance of $La_{0.7}Sr_{0.3}Mn_{1-x}O_3$ is optimized at intermediate Mo concentrations, where the balance between magnetic dilution and double-exchange enhancement favors efficient AC heating (Fig. 9).

Table 3 shows the magnetic hyperthermia performance of $La_{0.7}Sr_{0.3}Mn_{1-x}Mo_xO_3$ ($x = 0.10$, 0.15, 0.20) at a constant field of 23.873 kA m^{-1}. SAR increases with frequency for all samples, with $x = 0.10$ and 0.15 achieving the highest values (13.01 and 15.19 W g^{-1} at 313 kHz), indicating superior heating efficiency. In contrast, $x = 0.20$ shows significantly lower SAR (~6.68 W g^{-1}), reflecting weaker magnetic interactions due to higher Mo content. The ILP trend mirrors the SAR behavior, while the Curie temperature decreases with increasing Mo, correlating with reduced hyperthermia performance. These results suggest that intermediate Mo doping ($x = 0.10$–0.15) optimizes both heating efficiency and thermal response, making it most suitable for therapeutic applications.

In magnetic hyperthermia, the terms self-limited and self-regulated describe the temperature response of nanoparticles under an alternating magnetic field. Self-limited heating refers to the intrinsic property whereby heating naturally slows and levels off as the T_C is approached, occurring passively due to the loss of

Table 3 Specific absorption rate (SAR), intrinsic loss parameter (ILP), and Curie temperature (T_C) of $La_{0.7}Sr_{0.3}Mn_{1-x}Mo_xO_3$ samples measured at different frequencies under a constant magnetic field of 23.873 kA m^{-1}

Samples	H (kA m^{-1})	Frequency (kHz)	SAR (W g^{-1})	ILP (nHm/Kg)	T_C (K)
$La_{0.7}Sr_{0.3}Mn_{0.9}Mo_{0.1}O_3$	23.873	119	8.547	0.126	340
	23.873	203	12.256	0.105	340
	23.873	313	13.013	0.072	340
$La_{0.7}Sr_{0.3}Mn_{0.85}Mo_{0.15}O_3$	23.873	119	6.849	0.100	350
	23.873	203	8.876	0.076	350
	23.873	313	15.193	0.085	350
$La_{0.7}Sr_{0.3}Mn_{0.8}Mo_{0.2}O_3$	23.873	119	3.845	0.0567	290
	23.873	203	7.664	0.066	290
	23.873	313	6.678	0.037	290

ferromagnetic ordering, regardless of whether T_C lies within the therapeutic range.[30] In contrast, self-regulated heating occurs when T_C is deliberately tuned to fall within the hyperthermia window (~42–46 °C), enabling controlled and safe heating suitable for cancer therapy. In our Mo-doped LSMO series, T_C values span 16.85–76.85 °C. These nanoparticles exhibit self-limited behavior, with heating intrinsically constrained by T_C, while the current compositions do not fully achieve self-regulated heating in the therapeutic range. This distinction is critical for interpreting AC heating performance and provides a framework for future compositional tuning to optimize temperature-controlled hyperthermia.

7 Conclusion

This study demonstrates that Mo substitution in $La_{0.7}Sr_{0.3}Mn_{1-x}Mo_xO_3$ nanoparticles effectively tunes structural, microstructural, and magnetic properties relevant to magnetic hyperthermia. XRD and Rietveld analyses confirmed stable rhombohedral structures, with slight lattice expansion indicating successful Mo incorporation. SEM and crystallite analyses showed that higher Mo content reduces particle size and increases microstrain, reflecting Mo's influence on nucleation and growth. Magnetic measurements revealed tunable T_C and soft ferromagnetic behavior, while AC magnetic heating experiments indicated that intermediate Mo doping (x = 0.10–0.15) provides the highest specific absorption rates. All samples exhibited self-limited heating, with temperature rise intrinsically constrained by the T_C. However, the observed T_C are above the optimal hyperthermia window, suggesting that further tuning of composition, particle size, or morphology is required to achieve controlled, therapeutic self-regulated heating. Overall, these findings highlight the potential of Mo-substituted LSMO nanoparticles as a platform for self-limited magnetic hyperthermia. Future work could focus on fine-tuning Mo doping levels, controlling nanoparticle size and crystallinity, and tailoring surface properties to bring the Curie temperature closer to the therapeutic window and enhance SAR, thereby enabling safe and efficient temperature-regulated hyperthermia.

Conflicts of interest

There are no conflicts to declare.

Data availability

The data that support the findings of this study are available from the corresponding author upon reasonable request.

Acknowledgements

This work was supported by the Tunisian Ministry of Higher Education and Scientific Research.

References

1 R. K. Gilchrist, R. Medal, W. D. Shorey, R. C. Hanselman, J. C. Parrott and C. B. Taylor, Selective inductive heating of lymph nodes, *Ann. Surg.*, 1957, **146**, 596–606, DOI: 10.1097/00000658-195710000-00007.

2 K. Maier-Hauff, R. Rothe, R. Scholz, U. Gneveckow, P. Wust, B. Thiesen, A. Feussner, A. Deimling, N. Waldoefner, R. Felix and A. Jordan, Intracranial Thermotherapy using Magnetic Nanoparticles Combined with External Beam Radiotherapy: Results of a Feasibility Study on Patients with Glioblastoma Multiforme, *J. Neuro-Oncol.*, 2006, 53–60, DOI: 10.1007/S11060-006-9195-0.

3 C. Y. Foo, N. Munir, A. Kumaria, Q. Akhtar, C. J. Bullock, A. Narayanan and R. Z. Fu, Medical Device Advances in the Treatment of Glioblastoma, *Cancers*, 2022, **14**, 5341, DOI: 10.3390/CANCERS14215341.

4 A. Hervault and N. T. K. Thanh, Magnetic nanoparticle-based therapeutic agents for thermo-chemotherapy treatment of cancer, *Nanoscale*, 2014, **6**, 11553–11573, DOI: 10.1039/C4NR03482A.

5 D. T. Nguyen and K. S. Kim, Controlled Magnetic Properties of Iron Oxide-Based Nanoparticles for Smart Therapy, *KONA Powder Part. J.*, 2016, **33**, 33–47, DOI: 10.14356/KONA.2016010.

6 A. V. Pashchenko, N. A. Liedienov, I. V. Fesych, Q. Li, V. G. Pitsyuga, V. A. Turchenko, V. G. Pogrebnyak, B. Liu and G. G. Levchenko, Smart magnetic nanopowder based on the manganite perovskite for local hyperthermia, *RSC Adv.*, 2020, **10**, 30907–30916, DOI: 10.1039/D0RA06779B.

7 A. T. Apostolov, I. N. Apostolova and J. M. Wesselinowa, MO.Fe2O3 nanoparticles for self-controlled magnetic

hyperthermia, *J. Appl. Phys.*, 2011, **109**, 083939, DOI: 10.1063/1.3580476/929528.

8 M. Gerosa, M. Dal Grande, A. Busato, F. Vurro, B. Cisterna, E. Forlin, F. Gherlinzoni, G. Morana, M. Gottardi, P. Matteazzi, A. Speghini and P. Marzola, Nanoparticles exhibiting self-regulating temperature as innovative agents for Magnetic Fluid Hyperthermia, *Nanotheranostics*, 2021, **5**, 333, DOI: 10.7150/NTNO.55695.

9 Magnetic carbon nanotubes for self-regulating temperature hyperthermia – RSC Advances (RSC Publishing)DOI:DOI: 10.1039/C7RA13256E, https://pubs.rsc.org/en/content/articlehtml/2018/ra/c7ra13256e?utm_source=chatgpt.com (accessed November 12, 2025).

10 P. Guardia, A. Riedinger, H. Kakwere, F. Gazeau and T. Pellegrino, *Magnetic Nanoparticles for Magnetic Hyperthermia and Controlled Drug Delivery*, Wiley Blackwell, 2014, pp. 139–172, DOI: 10.1002/9783527675821.CH06.

11 C. S. S. R. Kumar and F. Mohammad, Magnetic nanomaterials for hyperthermia-based therapy and controlled drug delivery, *Adv. Drug Delivery Rev.*, 2011, **63**, 789–808, DOI: 10.1016/J.ADDR.2011.03.008.

12 M. Ahmadi, R. Ghomashchi, D. Vasjhaee, M. Ahmadi, R. Ghomashchi and D. Vasjhaee, A review on perovskite magnetic nanoparticles (MNPs) used in magnetic hyperthermia (HT), in *Proceedings of the 2nd International Electronic Conference on Metals*, 2025.

13 A. V. Pashchenko, N. A. Liedienov, I. V. Fesych, Q. Li, V. G. Pitsyuga, V. A. Turchenko, V. G. Pogrebnyak, B. Liu and G. G. Levchenko, Smart magnetic nanopowder based on the manganite perovskite for local hyperthermia, *RSC Adv.*, 2020, **10**, 30907–30916, DOI: 10.1039/D0RA06779B.

14 L. V. Bau and N. M. An, Magneto-electric properties and magnetic entropy change in perovskite La0.7Sr0.3Mn1−xTixO3, *J. Magn. Magn. Mater.*, 2016, **420**, 275–279, DOI: 10.1016/J.JMMM.2016.07.044.

15 N. Kallel, G. Dezanneau, J. Dhahri, M. Oumezzine and H. Vincent, Structure, magnetic and electrical behaviour of La0.7Sr0.3Mn1−xTixO3 with 0 <x <0.3, *J. Magn. Magn. Mater.*, 2003, **261**, 56–65, DOI: 10.1016/S0304-8853(02)01413-0.

16 P. Guardia, R. Di Corato, L. Lartigue, C. Wilhelm, A. Espinosa, M. Garcia-Hernandez, F. Gazeau, L. Manna and T. Pellegrino, Water-soluble iron oxide nanocubes with high values of specific absorption rate for cancer cell hyperthermia treatment, *ACS Nano*, 2012, **6**, 3080–3091, DOI: 10.1021/NN2048137/SUPPL_FILE/NN2048137_SI_001.PDF.

17 S. Murugan and M. Ashokkumar, Targeted cancer therapy through self-regulated magnetic hyperthermia using biocompatible zirconium-doped LSMO nanoparticles, *Chem. Eng. Sci.*, 2026, **321**, 122731, DOI: 10.1016/J.CES.2025.122731.

18 A. Ahmad, H. Akbar, I. Zada, F. Anjum, A. M. Afzal, S. Javed, M. Muneeb, A. Ali and J. R. Choi, Improvement of the Self-Controlled Hyperthermia Applications by Varying Gadolinium Doping in Lanthanum Strontium Manganite Nanoparticles, *Molecules*, 2023, **28**, 7860, DOI: 10.3390/MOLECULES28237860/S1.

19 Y. Shlapa, M. Kulyk, V. Kalita, T. Polek, A. Tovstolytkin, J. M. Greneche, S. Solopan and A. Belous, Iron-Doped (La,Sr)MnO3 Manganites as Promising Mediators of Self-Controlled Magnetic Nanohyperthermia, *Nanoscale Res. Lett.*, 2016, 1–8, DOI: 10.1186/S11671-015-1223-6.

20 J. Makni, K. Riahi, F. Ayadi, V. Nachbaur, W. Cheikhrouhou-Koubaa, M. Koubaa, M. A. Hamayun, E. K. Hlil and A. Cheikhrouhou, Evaluation of La0.7Sr0.3Mn1-xBxO3 (B=Mo, Ti) nanoparticles synthesized via GNP method for self-controlled hyperthermia, *J. Alloys Compd.*, 2018, **746**, 626–637, DOI: 10.1016/J.JALLCOM.2018.02.302.

21 R. Peng, X. Fan, Z. Jiang and C. Xia, Characteristics of La0.85Sr0.15MnO3–δ Powders Synthesized by a Glycine-Nitrate Process, *Fuel Cells*, 2006, **6**, 455–459, DOI: 10.1002/FUCE.200600009.

22 O. L. Lanier, O. I. Korotych, A. G. Monsalve, D. Wable, S. Savliwala, N. W. F. Grooms, C. Nacea, O. R. Tuitt and J. Dobson, Evaluation of magnetic nanoparticles for magnetic fluid hyperthermia, *Int. J. Hyperthermia*, 2019, **36**, 687–701, DOI: 10.1080/02656736.2019.1628313/SUPPL_FILE/IHYT_A_1628313_SM6585.PDF.

23 R. Epherre, E. Duguet, S. Mornet, E. Pollert, S. Louguet, S. Lecommandoux, C. Schatz and G. Goglio, Manganite perovskite nanoparticles for self-controlled magnetic fluid hyperthermia: about the suitability of an aqueous combustion synthesis route, *J. Mater. Chem.*, 2011, **21**, 4393–4401, DOI: 10.1039/C0JM03963B.

24 L. A. Chick, L. R. Pederson, G. D. Maupin, J. L. Bates, L. E. Thomas and G. J. Exarhos, Glycine-nitrate combustion synthesis of oxide ceramic powders, *Mater. Lett.*, 1990, **10**, 6–12, DOI: 10.1016/0167-577X(90)90003-5.

25 T. Roisnel and J. Rodríguez-Carvajal, WinPLOTR: A Windows Tool for Powder Diffraction Pattern Analysis, *Mater. Sci. Forum*, 2001, 378–381, DOI: 10.4028/WWW.SCIENTIFIC.NET/MSF.378-381.118.

26 H. M. Rietveld, A profile refinement method for nuclear and magnetic structures, *J. Appl. Crystallogr.*, 1969, **2**, 65–71, DOI: 10.1107/S0021889869006558.

27 G. K. Williamson and W. H. Hall, X-ray line broadening from filed aluminium and wolfram, *Acta Metall.*, 1953, **1**, 22–31, DOI: 10.1016/0001-6160(53)90006-6.

28 M. S. Kim, J. B. Yang, Q. Cai, X. D. Zhou, W. J. James, W. B. Yelon, P. E. Parris, D. Buddhikot and S. K. Malik, The effect of Cu-doping on the magnetic and transport properties of La0.7Sr0.3MnO3, *J. Appl. Phys.*, 2005, **97**, 10H714, DOI: 10.1063/1.1860992.

29 M. H. Phan and S. C. Yu, Review of the magnetocaloric effect in manganite materials, *J. Magn. Magn. Mater.*, 2007, **308**, 325–340, DOI: 10.1016/J.JMMM.2006.07.025.

30 G. Niraula, C. Wu, X. Yu, S. Malik, D. S. Verma, R. Yang, B. Zhao, S. Ding, W. Zhang and S. K. Sharma, The Curie temperature: a key playmaker in self-regulated temperature hyperthermia, *J. Mater. Chem. B*, 2024, **12**, 286–331, DOI: 10.1039/D3TB01437A.